The Namib Turbulence Experiment

Investigating Surface–Atmosphere Heat Transfer in Three Dimensions

Rainer V. J. Hilland, Christian Bernhofer, May Bohmann, Andreas Christen, Marwan Katurji, Gillian Maggs-Kölling, Matthias Krauß, Jarl A. Larsen, Eugene Marais, Andrea Pitacco, Benjamin Schumacher, Robert Spirig, Nadia Vendrame, and Roland Vogt

ABSTRACT: The Namib Turbulence Experiment (NamTEX) was a multinational micrometeorological campaign conducted in the central Namib Desert to investigate three-dimensional surface layer turbulence and the spatiotemporal patterns of heat transfer between the subsurface, surface, and atmosphere. The Namib provides an ideal location for fundamental research that revisits some key assumptions in micrometeorology that are implicitly included in the parameterizations describing energy exchange in weather forecasting and climate models: homogenous flat surfaces, no vegetation, little moisture, and cloud-free skies create a strong and consistent diurnal forcing, resulting in a wide range of atmospheric stabilities. A novel combination of instruments was used to simultaneously measure variables and processes relevant to heat transfer: a 3-km fiber-optic distributed temperature sensor (DTS) was suspended in a pseudo-three-dimensional array within a 300 m × 300 m domain to provide vertical cross sections of air temperature fluctuations. Aerial and ground-based thermal imagers recorded high-resolution surface temperature fluctuations within the domain and revealed the spatial thermal imprint of atmospheric structures responsible for heat exchange. High-resolution soil temperature and moisture profiles together with heat flux plates provided information on near-surface soil dynamics. Turbulent heat exchange was measured with a vertical array of five eddy-covariance point measurements on a 21-m mast, as well as by collocated small- and large-aperture scintillometers. This contribution first details the scientific goals and experimental setup of the NamTEX campaign. Then, using a typical day, we demonstrate (i) the coupling of surface layer, surface, and soil temperatures using high-frequency temperature measurements, (ii) differences in spatial and temporal standard deviations of the horizontal temperature field using spatially distributed measurements, and (iii) horizontal anisotropy of the turbulent temperature field.

KEYWORDS: Atmosphere; Africa; Atmosphere-land interaction; Turbulence; Energy budget/balance

AFFILIATIONS: Hilland, Bohmann, and Christen—Environmental Meteorology, Institute of Earth and Environmental Sciences, University of Freiburg, Freiburg, Germany; **Bernhofer**—Institute of Hydrology and Meteorology, Technical University of Dresden, Dresden, Germany; **Katurji and Schumacher**—School of Earth and Environment, University of Canterbury, Christchurch, New Zealand; **Maggs-Kölling and Marais**—Gobabeb Namib Research Institute, Walvis Bay, Namibia; **Krauß**—InfraTec GmbH, Dresden, Germany; **Larsen, Spirig, and Vogt**—Department of Environmental Sciences, Atmospheric Sciences, University of Basel, Basel, Switzerland; **Pitacco and Vendrame***—Department of Agronomy, Food, Natural Resources, Animals and Environment, University of Padua, Padua, Italy
* CURRENT AFFILIATION: Center Agriculture Food Environment, University of Trento, Trento, Italy

T he vertical transfer of heat between the subsurface, surface, and the atmosphere is of fundamental importance to predict weather and simulate climate dynamics in numerical models (ECMWF 1988). Energy exchange at the surface interface controls boundary layer development, affects cloud formation, and results in local to global wind systems (Stull 1988). In most applications, individual realizations of the temperature field and the detailed structure of the heat transfer at any point and time are not used, but rather the integral outcome over a certain time period or spatial domain such as a model grid cell. Hence, to calculate heat transfer between the land surface and the atmosphere computationally efficiently in numerical models, many processes (e.g., turbulent motions) are not resolved and dynamical three-dimensional processes are simplified to quasi steady-state one-dimensional problems (Garratt and Pielke 1989). Generally, this is justified by assuming horizontal homogeneity/ isotropy and short-term stationarity of the temperature fields in the subsurface, at the surface and in the atmospheric surface layer (Kaimal and Finnigan 1994).

Rigorous micrometeorological measurements are key to derive and evaluate the capabilities and limits of underlying assumptions in heat transfer parameterizations for models. As it is difficult to establish spatially distributed measurement arrays, most measurements of temperature fluctuations and sensible heat flux dynamics at the surface–atmosphere interface are done at a single location and resolve only the time domain. Using the ergodic hypothesis, measurements in the time domain are then, under the assumption of horizontal homogeneity and stationarity, translated into spatially integrated measurements.

Nevertheless, the few detailed measurements of the spatial nature of turbulent heat transfer near the land–atmosphere interface reveal complex and partially self-organizing patterns (Schols 1984; Garai and Kleissl 2013). Persistent and fluctuating structures are found across a range of time and space scales from days to subseconds and from kilometers to millimeters. It has been long reported that the ergodic hypothesis may not be universally applicable across all scales (Tong 1996; Higgins et al. 2012). Further, failure of the fundamental homogeneity assumption has been discussed as a possible contributor to the energy balance closure problem (Mauder et al. 2020). Even at small scales (~10 m) over homogeneous surfaces, heterogeneities in the turbulent flow question the accuracy of one-dimensional treatments. Engelmann and Bernhofer (2016) investigated temporal and spatial fluxes in the Namib using a spatially distributed matrix of sonic anemometers and found temporal averaging alone underestimated fluxes compared to temporal and spatial averaging.

Multiple recent micrometeorological observation campaigns have been focused on intensive 3D observation of the boundary layer to improve understanding and model representation

of specific processes at the subgrid scale, e.g., Boundary-Layer Late Afternoon and Sunset Turbulence (BLLAST; Lothon et al. 2014) to investigate the afternoon transition period and Chequamegon Heterogeneous Ecosystem Energy-Balance Study Enabled by a High-Density Extensive Array of Detectors 2019 (CHEESEHEAD19; Butterworth et al. 2021) for heterogenous vegetated surface cover. In the IPAQS campaign Morrison et al. (2021) combined high-resolution and spatially distributed atmospheric, surface, and subsurface measurements at an idealized desert field site in Utah, United States, to investigate the spatial variability of the surface sensible heat flux and test simplifying assumptions in the surface energy balance equation over a homogenous surface. In addition, there are a few recent micrometeorological studies that targeted the dynamics of spatial air temperature fields using fiber-optic systems (e.g., Thomas et al. 2012; Zeeman et al. 2015; Zeller et al. 2021). Time-sequential thermography has also been used to investigate the rapidly changing spatial pattern of surface temperatures (e.g., Garai and Kleissl 2013; Morrison et al. 2017; Alekseychik et al. 2021).

The Namib Turbulence Experiment (NamTEX) provided a unique micrometeorological dataset in the central Namib Desert in March 2020. Using a combination of surface thermography, spatially resolving measurements of air temperature, subsurface measurements at the microscale, and spatial and temporally integrating heat flux measurements, NamTEX provides multidimensional data acquisition of near-surface turbulence and energy flux. This dataset allows for the investigation of the turbulent motions that control the spatiotemporal patterns of heat transfer between the (sub)surface and atmosphere.

Research goals

This contribution details the scientific goals and experimental setup of NamTEX and presents initial results to illustrate the capabilities of spatially resolved measurement and analysis methods. The experiment had the following goals with the corresponding research questions:

1. *To revisit the assumptions of one-dimensional and quasi-steady-state treatment of heat transfer at an ideal, homogeneous land surface*: What are the dominant spatial and temporal scales that couple subsurface, surface, and atmosphere and do they justify an integral steady state? Under which conditions is a one-dimensional treatment of the coupling of subsurface, surface, and atmosphere supported? Are there conditions when it fails?
2. *To investigate the linkage between the atmospheric flow field and the temperature field*: How are subsurface, surface, and atmospheric temperature dynamics coupled with the dynamics of the airflow near the surface? Can temperature fluctuations in the air and at the surface and subsurface be used as tracers for the coherence and penetration of turbulent eddies? How is the coherent movement of temperature fluctuations in space explained and linked to temporally integrated heat fluxes?
3. *To investigate the equivalency between spatial and temporal variation in temperature fluctuations relevant to heat transfer*: Are statistics derived in time and space always interchangeable across all scales? Can heat fluxes be inferred from spatial fluctuations and temporal fluctuations alike?
4. *To revisit the assumption of a horizontally isotropic and random field of heat transfer*: How is the heat transfer manifested in spatial patterns and coherent units of subsurface, surface, and air temperature fluctuations and resulting heat fluxes? Are there violations of the assumptions of horizontal isotropy and randomness due to self-organizing structures, submesoscale features, or a general horizontal anisotropy?

The Namib Desert

Due to the fundamental nature of the research questions, a site with a flat, horizontally homogeneous surface cover and negligible latent heat transfer was needed to fulfill standard

theoretical assumptions and avoid complications. The central Namib, on the southwestern coast of the African continent and reaching approximately 200 km inland, is one of the driest places on Earth (Mendelsohn et al. 2002) and fulfills these criteria. The NamTEX field site (23.516°S, 15.089°E, local noon about 1100 UTC) was located on a flat area in the central Namib 7 km northeast from the Gobabeb Namib Research Institute and Kuiseb River. On a regional scale, the surface sloped gradually downward to the west (Fig. 1, left). The site itself was flat and provided horizontally homogeneous surface cover on the order of many kilometers, a generally cloud-free atmosphere, regular and repeatable diurnal meteorology, strong solar forcing, and a wide range of atmospheric stabilities. The extreme dryness simplifies the energy budget calculations as latent heat flux is negligible (see section "Meteorological conditions").

The soil at the NamTEX site was composed of densely packed fine sand (prevailing diameter ~100 μm) covered by quartz granules and cobbles, with occasional small tufts of dead grass the only vegetation. A surface aerodynamic roughness length of 0.88 mm (±0.36 mm) was calculated from the sonic anemometer profile in neutral atmospheric stability conditions. This agrees well with both field and laboratory measurements of similar desert surfaces (Xian et al. 2002). Due to the absence of vegetation, there are no complicating effects due to biospheric controls or mechanical effects (e.g., moving grass).

Experimental design

The fundamental design principles of the campaign were to sample temperature fluctuations in both space and time, and in three dimensions in the atmospheric surface layer (ASL), at the surface, and in the subsurface. For example, thermal imagery captured from an unmanned aerial system (UAS) was used to measure radiometric surface brightness temperatures while a fiber-optic distributed temperature sensor (DTS) within the UAS field of view (FOV) measured space–time air temperatures (see Table 1 for a list of variables and abbreviations). At three locations within the same domain, dense thermocouple profiles measured vertical temperature
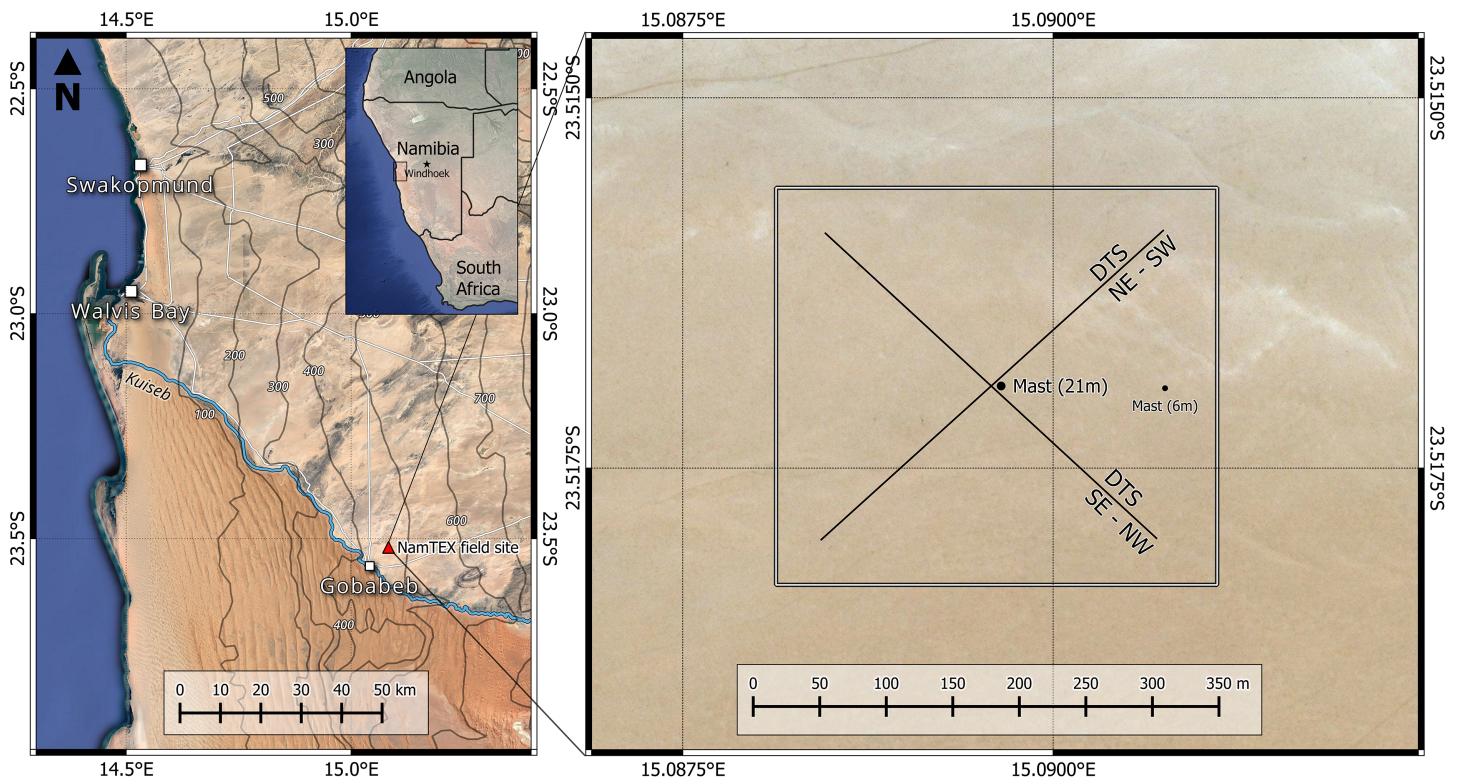

Fig. 1. (left) Location of the NamTEX field site in relation to Gobabeb, the Kuiseb River, and the Namib Sand Sea. **(right)** Close-up of the field site with outline of NamTEX domain. Map background from Google Earth (at left) and Bing (at right).

Table 1. List of variables and abbreviations.

Variable/above ground level	Description	Variable/ abbreviation	Description
ASL	Atmospheric surface layer	A-TIV	Adaptive thermal image velocimetry
C_n^2	Structure parameter of the refractive index of air (m$^{-2/3}$)	DTS	Distributed temperature sensor
FOV	Field of view	L	Obukhov Length (m)
LD	Downwelling longwave radiation (W m^{-2})	LU	Upwelling longwave radiation (W m^{-2})
LAS	Large-aperture scintillometer	NamTEX	Namib Turbulence Experiment
Q_E	Latent heat flux (W m^{-2})	Q_G	Ground heat flux (W m^{-2})
Q_H	Sensible heat flux (W m^{-2})	Q^*	Net surface energy balance (W m^{-2})
RH	Relative humidity (%)	S1–3	Soil sites 1, 2, 3 (Fig. 2)
SAS	Small-aperture scintillometer	SD	Downwelling shortwave radiation (W m^{-2})
σ_T	Standard deviation of temperature (K)	SR	Sunrise
SS	Sunset	SU	Upwelling shortwave radiation (W m^{-2})
T_{air}	Air temperature (°C)	T_{soil}	Soil/subsurface temperature (°C)
T_{surf}	Surface temperature (°C)	T'_{surf}	Surface temperature fluctuation from a (spatio-)temporal mean (°C)
UAS	Unmanned aerial system	u	Longitudinal wind component (m s^{-1})
v	Lateral wind component (m s^{-1})	w	Vertical wind component (m s^{-1})
ζ	Obukhov stability parameter		

gradients in the topsoil. Figure 2 shows a schematic overview of the measurement systems deployed during the campaign and their spatial arrangement within the field domain.

Taken together, these individual measurement systems create a pseudo-three-dimensional temperature measurement array complemented by space- and time-averaging heat flux instruments and traditional micrometeorological and energy balance measurement systems.

Air temperatures. The spatial distribution of turbulent temperature fluctuations was measured with a fiber-optic distributed temperature sensor (DTS), which provides the ability
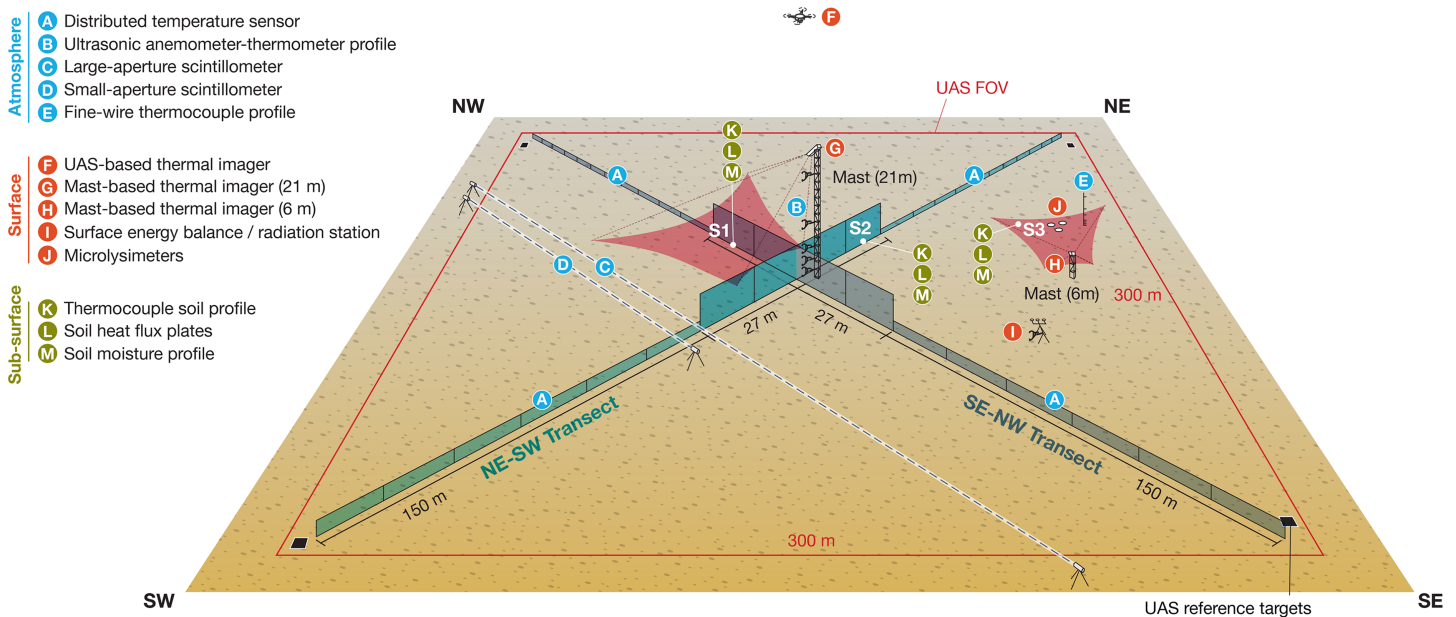

Fig. 2. Schematic overview of the NamTEX domain (not to scale). Letters refer to instruments and systems described in Table 2. Red areas approximate the FOVs of the thermal imagers. DTS transects are presented as 2D planes for illustrative purposes but are comprised of multiple thin horizontal transects (see sidebar "Resolving turbulent structures with DTS").

to measure temperature densely in both space and time (Thomas and Selker 2021). The fiber-optic DTS was arranged in two vertical cross-sectional planes in northeast–southwest and southeast–northwest orientations between opposing corners of the domain, forming a cross in plan view (see Fig. 1 and A in Fig. 2). The DTS sampled at 0.76 Hz (effective) and every 0.254 m across the length of the cable. A key motivator of the cross arrangement is the ability to interrogate the temperature field simultaneously in two axes (e.g., along and cross-wind). The DTS cable temperatures were converted to air temperatures by correcting for the significant radiative error according to Sigmund et al. (2017). More details on DTS measurements can be found in the sidebar "Resolving turbulent structures with DTS."

Surface heat fluxes. In the center of the domain on a 21-m mast, collocated with the intersection of the DTS axes was a vertical profile of four sonic anemometer–thermometers at 0.5, 1.0, 2.0, and 3.0 m AGL, and a combined sonic anemometer–thermometer and infrared gas analyzer at 12.0 m (B in Fig. 2). Sonic anemometry provides high-frequency (60 Hz) measurements of the three-dimensional wind vector and air density. It is a standard instrument for calculating surface sensible heat fluxes (and latent heat fluxes when paired with an appropriate sensor) using the eddy covariance method (Aubinet et al. 2012). EddyPro (v7.0.6) software was used to derive sensible heat fluxes (all heights) and the latent heat flux (12.0 m) with a 15-min averaging period (confirmed via Ogive test), and apply standard corrections (i.e., two-axis coordinate rotation, despiking, etc.).

Collocated large- (LAS) and small-aperture (SAS) scintillometers were installed to provide spatially integrated sensible heat flux measurements (C and D in Fig. 2). A scintillometer consists of a transmitter and receiver of electromagnetic waves emitted over a given pathlength and relates changes in the refractive index over this path to the sensible heat flux via Monin–Obukhov similarity theory (Thiermann and Grassl 1992; Ward 2017). Scintillometry provides an estimate of the sensible heat flux integrated over space as opposed to the eddy covariance method which measures at one point and integrates over time. Despite their different measurement principles, comparison of these two methods may be used to investigate hypotheses relating to the equivalence and convergence of the sensible heat flux in the space and time domains. Furthermore, the collocation of two scintillometers with differing pathlengths provides redundancy in the measurements. For the SAS measurements presented below, fluxes were derived using software provided by the manufacturer (SLSRun v2.35), which uses the scaling functions from Thiermann and Grassl (1992). Stability was determined on a 1-min basis from the 2.0-m sonic anemometer, and the friction velocity was derived internally by the SAS.

Surface thermography. At the interface between atmosphere and soil, the spatial distribution of surface temperature can be employed to understand both heterogeneities in the ground heat flux (e.g., Morrison et al. 2017) as well as the atmospheric structures transferring sensible heat into the air (e.g., Garai and Kleissl 2011; Garai et al. 2013). NamTEX employed three thermal imagers: two high-resolution mast-mounted imagers sampling continuously at 1 Hz (G in Fig. 2) and 0.2 Hz (H in Fig. 2) and collocated with specific subsets of the NamTEX domain, and a lower-resolution imager sampling discontinuously from a UAS-based platform (F in Fig. 2) encompassing the entire domain. For the latter, 88 flights were conducted, each 10–12 min in length. Flights consisted of hovering directly above the central mast at 425 m AGL as long as the battery and wind conditions would allow. Flights were spread throughout the diurnal course to capture the widest possible range of atmospheric stabilities. The thermography from all imagers was corrected for geometric distortion effects and the UAS-based imagery was stabilized using low-emissivity reference targets using the Blender animation software (Schumacher et al. 2019).

Resolving turbulent structures with DTS

A historical challenge in micrometeorological field research has been the difficulty and expense of spatially distributed measurement arrays. Although there have been previous attempts to infer horizontally separated measurements of high-frequency wind (Wilson 2013; Horst et al. 2004), wind and temperature (Engelmann and Bernhofer 2016), or just temperature (Everard et al. 2020) at small scales, those attempts have provided limited resolution and scale. Fiber-optic distributed temperature sensors are a comparatively simple and cost-effective method of obtaining thousands of individual temperature measurements.

A DTS consists of one or more fiber-optic cables, a measurement and control unit, and warm and cold calibration baths. A laser within the measurement unit is fired along the fiber and the spectrum of back-scattered light is analyzed. The ratio of Stokes to anti-Stokes in the back-scattered spectrum is proportional to the temperature of the cable and the distance along the cable is determined from the speed of light (Selker et al. 2006). DTS has been typically used for monitoring applications in, e.g., the oil and gas industry, in which longer sample times (≥1 min), spatial intervals (≥1 m), and cable lengths (up to 30,000 m) are suitable.

Within the last 10 years, technical advances have facilitated more rapid acquisition times (≈1 s) over smaller distances (0.254 m) using cables up to 5,000 m. These improvements have made DTS feasible for turbulence scales in the boundary layer (Thomas et al. 2012) and it has been employed to study specific phenomena such as nocturnal cold-air pooling (Zeeman et al. 2015), the applicability of Taylor's hypothesis (Cheng et al. 2017), mixing processes above a forest canopy (Peltola et al. 2021), and the structure and temporal evolution of the atmospheric boundary layer (Keller et al. 2011; Higgins et al. 2018). The possibilities of optical fiber sensing are vast, and the technique has been used for spatially distributed measurement of not only air temperature, but also air humidity (Schilperoort et al. 2018) and wind speed (Sayde et al. 2015), among others.

In NamTEX, two cable arrangements are distinguished within each cross section: a "dense" section at the cross intersection of 16 measurement transects, each 27 m horizontally and separated vertically by 0.17 m from 0.28 m above the surface to 2.85 m, and a "long" section of 327 m horizontal at two measurement heights (0.28 and 0.45 m above surface; see Fig. SB1a). The dense section provides a 0.254 m × 0.17 m measurement grid from which the vertical structure of individual heat-transferring turbulent elements may be observed, while the long section provides a larger area of the instantaneous horizontal temperature field (shown in Fig. 7).

Calibration of the DTS measurements was facilitated by thermally insulated warm (ambient) and cold baths (twice-daily refilled ice–water mixture) fitted with small aquarium pumps to avoid thermal stratification. These baths provide a comparatively stable reference temperature above and below the air temperature for use in calibration (des Tombe et al. 2020). Calibration of the temperatures was performed using the open source "dtscalibration" Python package (des Tombe and Schilperoort 2020). An energy balance was calculated for the cable to account for the radiative error and convective cooling following the method described by Sigmund et al. (2017).

Applying DTS to atmospheric measurements brings many challenges, including but not limited to the high degree of difficulty in installing the instrument and maintaining the calibration baths (especially so in a hostile environment like the Namib), the accurate spatial referencing of custom arrays, and the radiation error on the cable. In return, however, it offers a high degree of customizability and extraordinary spatial density.
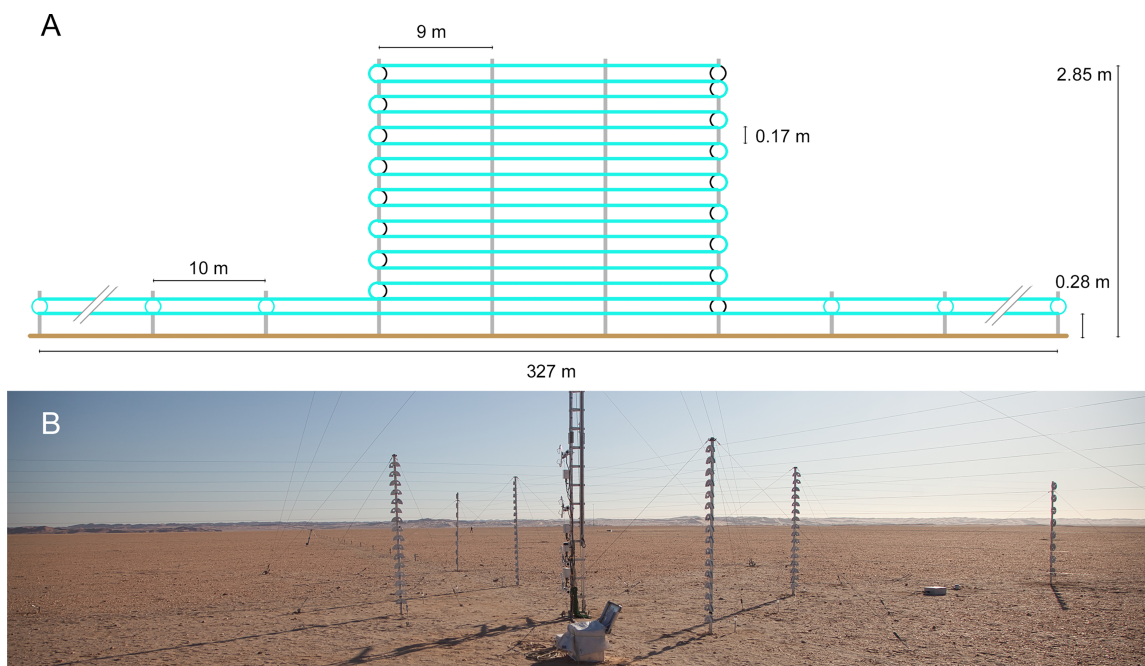

Fig. SB1. (a) Schematic of the arrangement of a single axis of the DTS (not to scale). (b) Photo of the installed dense section facing southwest. The large mast in the center supports sonic anemometers but is not used in the suspension of the DTS cable.

Surface radiation balance. A multi-instrument platform (I in Fig. 2) measured additional micrometeorological variables including shortwave and longwave incident and outgoing radiative fluxes, air temperature and humidity. Components of the net radiation were adjusted to the measurements of the nearby Baseline Surface Radiation Network and for net radiation resulted in agreement within ±2% or ±10 W m^{-2}, whichever is larger. An additional sonic anemometer–thermometer was also located at the platform.

Subsurface temperature and heat transfer measurements. The energy balance at the surface drives and is driven by temperature gradients within the soil. Soil temperature and heat fluxes are commonly sampled at a low rate (e.g., 60 s–5 min), and several centimeters below the surface. However, heavy radiation load together with low soil thermal conductivity and heat capacity produce very steep gradients close to the surface and a highly dynamic skin temperature. To observe the propagation of high-frequency temperature fluctuations into the soil, high-resolution soil temperature profiles were measured via vertical thermocouple arrays at three locations (K in Fig. 2), hereafter referred to as S1, S2, and S3. At each location 25 thermocouples in a single vertical profile were spaced densely near the surface and at increasing vertical distance with depth, ranging from 0 to –203 mm (see Table 2) and sampled at high frequency (1 Hz). Soil heat fluxes were also observed using thermoelectric heat-flux plates at –50 and –100 mm (S1, S2, S3) and –200 mm (S3). Water potential was measured at –50 mm at all three soil sites at 1-min intervals.

Additionally, three microlysimeters were deployed (J in Fig. 2) to measure potential deposition of fog water during nocturnal fog events and to estimate evaporation (Feigenwinter et al. 2020).

Time synchronization. The dataloggers and most measurement system clocks were actively synced via GPS. The dataloggers used Garmin GPS16X-HVS receivers (Garmin Ltd., Lenexa, Kansas, United States) to sync the time every 30 min. The DTS and thermal imagers were synced with NaviLock NL-8012U USB GPS receivers (NaviLock, Berlin, Germany) and the NMEATime2 software (v2.2.1, VisualGPS). The UAS thermography was equipped with a GPS time sync but this failed after two days. Subsequently the UAS thermography was synced manually to UTC time and has an assumed error of ±1 s. The scintillometer computers were not actively synced in the field and had a time error of <10 s at the end of the campaign.

Meteorological conditions

The NamTEX campaign ran continuously from 8 to 16 March 2020 (late summer in the Namib). During this period the prevailing meteorological conditions allowed for consistently similar diurnal patterns (Fig. 3). The incident shortwave radiative flux at the site demonstrates eight consecutive days of cloud-free conditions and strong, repeated surface radiative forcing. This diurnal cycle of strong surface radiative heating during the day (surface temperatures reached a sustained daily T_{max} of 53.9°–61.3°C) and cooling at night (average sustained daily surface T_{min} of 10.4°–16.9°C) created regular periods of highly unstable and stable atmospheric conditions. Air temperatures at 2 m AGL reached sustained daily highs of 32.1°–37.1°C. High surface albedo and surface temperature lead to a moderate net radiation balance despite strong shortwave forcing. Net all-wave radiation of the 8 days ranged from a minimum of –102 W m^{-2} to a maximum of 462 W m^{-2}. One exception was a brief period around sunrise on March 16 when dense fog occurred at the site. Specific humidity over the period (2 m AGL) was between 2 and 10 g kg^{-1} (mean 7 g kg^{-1}). The low soil volumetric water content from 4% (–100 mm) to 1% (–500 mm) and the Bowen ratio of the average fluxes of 55 highlight the extreme dryness during the measurement period.

Similar regularity was observed in a persistent wind regime, which reflects the interplay between thermo-topographic wind systems (Tyson and Seely 1980). Most days (8–15 March)

Table 2. Instrumentation overview. Location letters refer to Fig. 2. Superscripts define the method of time synchronization: 1) actively synced via GPS, 2) unsynced, 3) manually synced to UTC. See "Time synchronization" section for details.

| Instrument or system (abbreviation)	Model	Manufacturer	Location (Fig. 2) and height	Variable(s)	Configuration
Atmospheric measurements					
Distributed Temperature Sensor (DTS)[1]	Ultima-S	Silixa Ltd. (Elstree, United Kingdom)	A: arrangement details in "Resolving turbulent structures with DTS" sidebar	T_{air} (°C)	0.76 Hz; 0.254 m
Sonic anemometer–thermometer profile [with infrared gas analyser][1]	CSAT-3 IRGASON	Campbell Scientific (Logan, UT, United States)	B: 0.5, 1.0, 2.0, 3.0 m AGL B: 12.0 m AGL	u, v, w (m s⁻¹), T_{air} (°C, acoustic) u, v, w (m s⁻¹), T_{air} (°C, acoustic), H_2O, CO_2 (g m⁻³)	60-Hz internal sampling, 20-Hz data output
Large-aperture scintillometer (LAS)[2]	BLS900	Scintec AG (Rottenburg, Germany)	C: 1.7 m AGL	Q_H (W m⁻²) [derived from direct measurement of C_n^2 (m⁻²/³)]	Pathlength 300 m; path reduction aperture disks
Small-aperture scintillometer (SAS)[2]	SLS20		D: 1.7 m AGL		Pathlength 155 m
Fine-wire thermocouple profile[1]	FW03 75 μm	Campbell Scientific (Logan, UT, United States)	E: 0.0, 0.02, 0.05, 0.1, 0.2, 0.5, 1.0, 2.0 m AGL	T_{air} (°C)	0.2 Hz
Surface measurements					
UAS-based thermal imager[3]	Vue Pro R 640	FLIR Systems (Wilsonville OR, United States)	F: UAS, flight level ~425 m AGL	T_{surf} (°C, radiometric)	7.5 Hz discontinuous
Mast-based (21 m) thermal imager[1]	VarioCAM HD	InfraTec GmbH (Dresden, Germany)	G: 21 m AGL	T_{surf} (°C, radiometric)	1 Hz continuous
Mast-based (6 m) thermal imager[1]	VarioCAM HD		H: 6 m AGL	T_{surf} (°C, radiometric)	0.2 Hz continuous
Surface energy balance/radiation station[1]	NR01 4-component net radiometer	Hukseflux (Delft, Netherlands)	I: 2 m AGL	SU, SD, LU, LD (W m⁻²)	0.5-Hz sample, 60-s average output
	CSAT-3 ultrasonic anemometer–thermometer	Campbell Scientific (Logan, UT, United States)		u, v, w (m s⁻¹), T_{air} (°C, acoustic)	60-Hz internal sampling, 20-Hz data output
	HMP155 temperature and humidity probe	Vaisala (Vantaa, Finland)		T_{air} (°C), RH (%)	0.5-Hz sample, 60-s average output, radiation shield, nonventilated
Microlysimeter[1]	Custom-made (Feigenwinter et al. 2020)		J (×3)	Soil weight (g)	1-Hz internal sampling, 60-s output
Subsurface measurements					
Thermocouple soil profiles[1]	SRTC-EI-30 (Type-E, 0.25 mm diameter)	Omega Engineering (Norwalk, CO, United States)	K: 0.0, −2.5, −5.0, −7.5, −10.0, −12.5, −15.0, −18.0, −20.5, −25.5, −30.5, −35.5, −40.5, −45.5, −51.0, −61.0, −71.0, −81.0, −91.5, −101.5, −122.0, −142.0, −162.5, −183.0, −203.0 mm (×3)	T_{soil} (°C)	1 Hz
Soil heat flux plates[1]	HFT3	REBS Inc. (Seattle, WA, United States)	L: −5 cm (×3)	Q_G (W m⁻²)	1 Hz
	Rimco CN3	McVan Instruments (Mulgrave, Australia)	L: −10 cm (×3)		
Soil moisture profile[1]	SoilVUE10	Campbell Scientific (Logan, UT, United States)	M: −0.05, −0.10, −0.20, −0.30, −0.40, −0.50 m (×3)	T_{soil} (°C), Q_G (W m⁻²), volumetric water content (%)	0.2 Hz
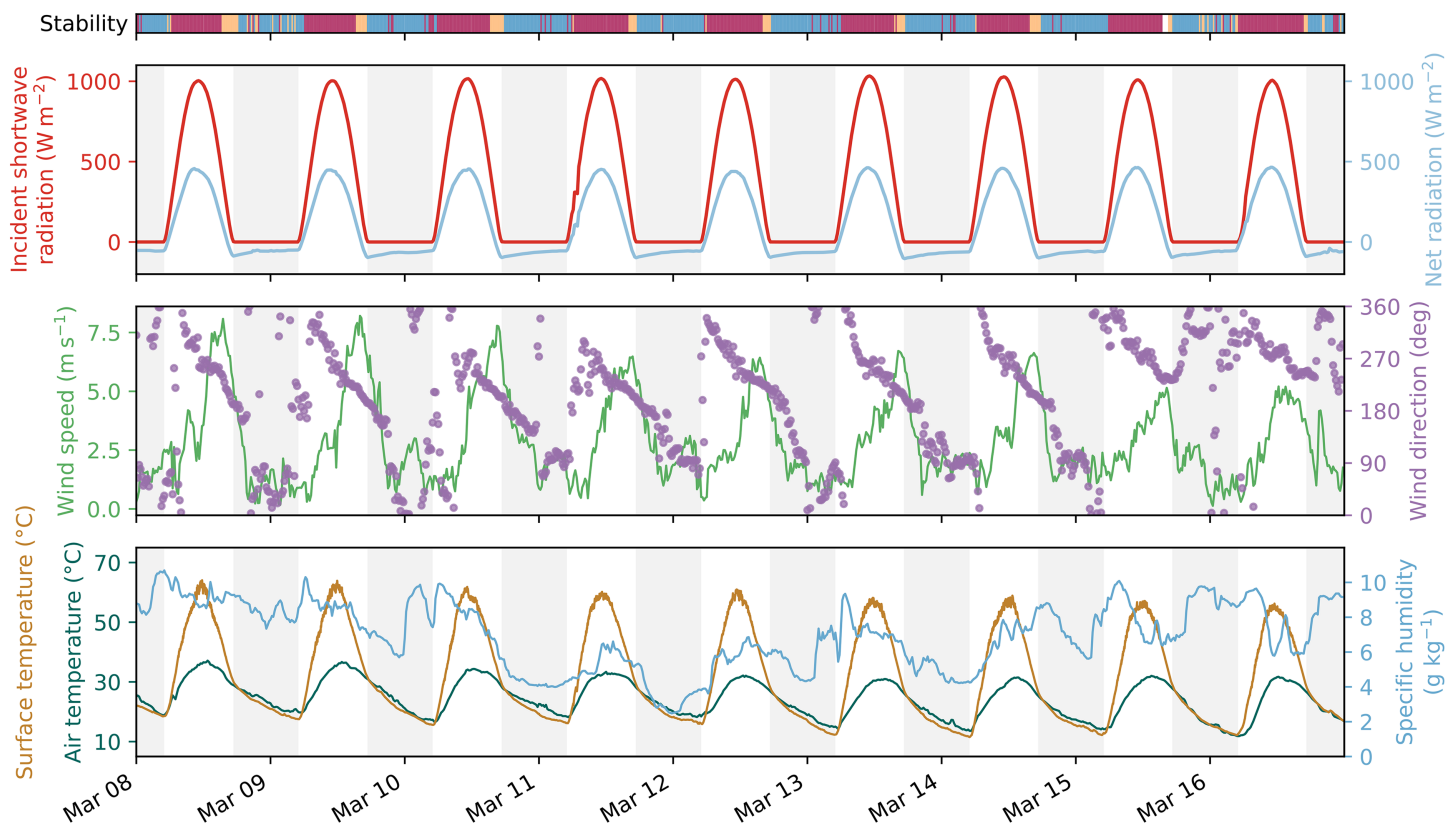
Fig. 3. Conditions at the NamTEX site throughout the observation period (15-min averages). The uppermost bar shows stability classes calculated from the 3.0-m sonic anemometer. Red (free convection): $-\infty < \zeta \leq -0.1$; orange (unstable): $-0.1 < \zeta < 0$; blue (stable): $0 \leq \zeta < \infty$; ζ is the stability parameter according to Obukhov). Incident shortwave radiation, net radiation, and air temperature measurements are from the surface energy balance station (I in Fig. 2), wind speed and direction measured at 12.0 m (A in Fig. 2), surface temperature calculated from a 25-pixel average of the 21-m thermal imager (H in Fig. 2) using an emissivity of 0.88 (Göttsche et al. 2018).

begin with northerly winds of 1–3 m s^{-1} (12 m AGL) at sunrise and rotate counterclockwise toward the southwest through the course of the day, reaching 6–9 m s^{-1} after solar noon. During nighttime moderate winds blow from the east. The final two days show a change in wind regime in which the wind rotates back to the northwest direction after sunset. This situation is typically connected to inland advection of stratus/fog (Spirig et al. 2019).

One-dimensional heat transfer

To address research goals 1 and 2, we first present heat transfer in a classical one-dimensional approach using vertically aligned subsurface (S1) and air (DTS) temperature measurements from a typical day (Fig. 4). The subsurface temperatures illustrate the intense gradients that develop in the upper centimeters of the desert soil. The diurnal amplitude of nearly 50 K at the surface (0 mm) is reduced to just 4 K at a soil depth of 200 mm. The air temperatures of the lowest (0.28 m) and highest (2.85 m) vertically aligned DTS measurements show a diurnal amplitude of 26 and 21 K, respectively.

The changing intensity of turbulent motion through the day is reflected in the subsurface and air temperature standard deviations. The influence of turbulent fluctuations on the surface temperature diminishes rapidly with depth, but slight fluctuations are still observed on the 15-min time scale at depths of 10–25 mm. Also presented is the surface energy balance for the day. The ground and sensible heat fluxes alone provide 89% energy balance closure on the day.

The small latent heat flux calculated at the central mast was complicated by frequent periods in which the derived flux was flagged as unsuitable for analysis per Mauder and Foken (2004). Given the regularity of conditions, a campaign-average diurnal latent heat flux was
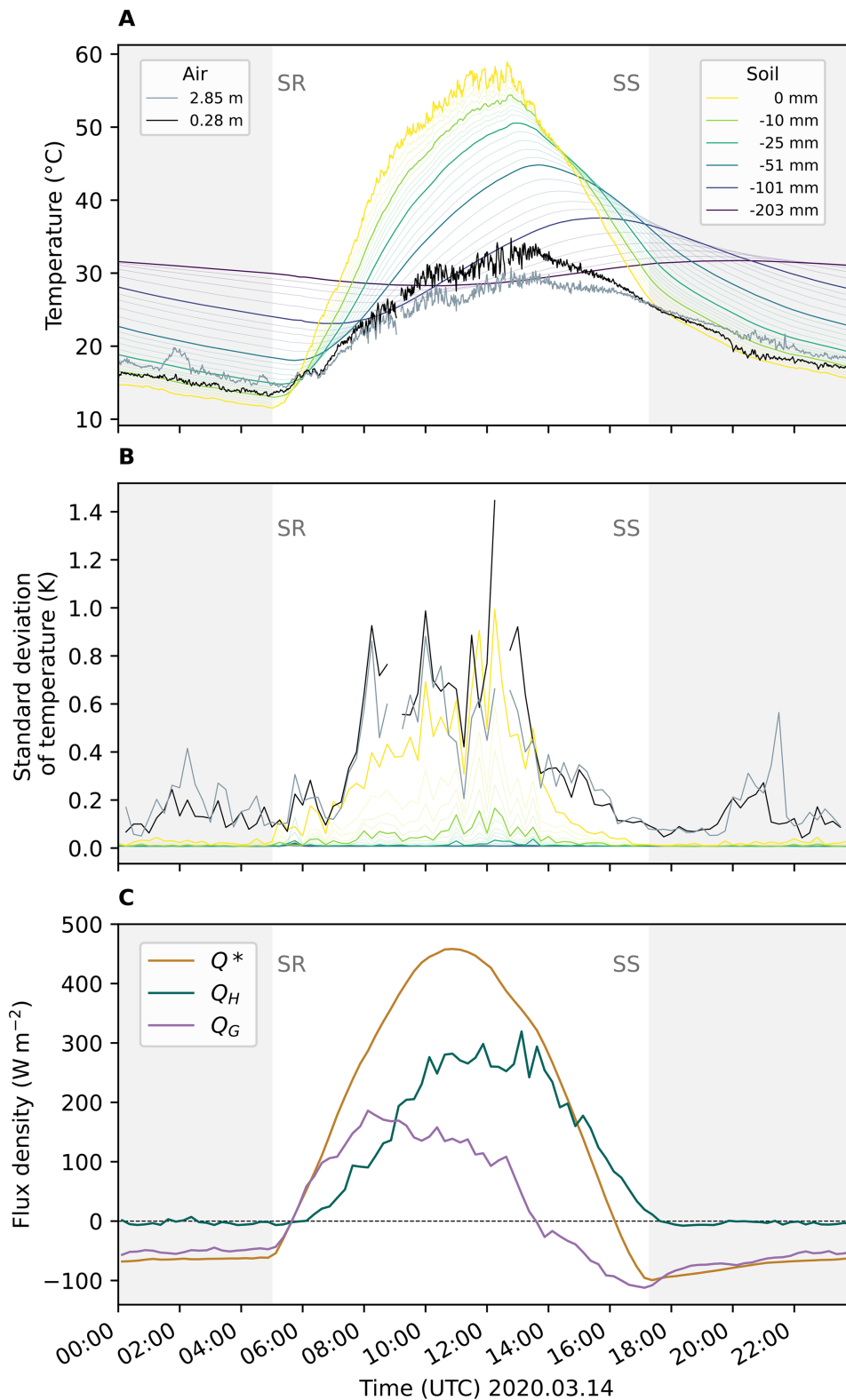
Fig. 4. Time series for 14 Mar. (a) 1-min averaged subsurface temperatures (S1) and vertically aligned air temperatures (DTS). Only the highest and lowest DTS transects are plotted for clarity. (b) 15-min linearly detrended standard deviations of the time series in panel (a). (c) Surface energy balance, 15-min averaging period. Net radiation Q^* from the surface energy balance station (I in Fig. 2), ground heat flux Q_G measured from the soil heat flux plate with storage calculated via the thermocouple profile using a volumetric heat capacity of 1.28 MJ m^{-3} K^{-1}, and turbulent sensible heat flux Q_H calculated from the central-mast sonic anemometer at 2.0 m AGL. The latent heat flux Q_E is not considered due to its low value (daily average $Q_E = 0 \pm 6$ W m^{-2}), neither is the small storage related flux from temperature and humidity changes between the surface and height of the net radiometer.

determined by averaging only good-quality fluxes, binned by time. The resulting average flux of 0 ± 6 W m^{-2} improves energy balance closure by only 1%.

The temperature spectra shown in Fig. 5a illustrate both the commonalities and differences between the heat transfer in soil and atmosphere by resolving the contribution of individual frequencies to the full time series via a Fourier transform. All see the highest variance at the 24-h scale as expected due to the solar forcing that causes the large diurnal amplitudes of temperatures. Both the air and remotely sensed surface temperatures show an inertial subrange, given by the $f^{-5/3}$ slope, though the air temperature only reaches this slope at the highest frequencies (approximately 1–8 Hz) suggesting that there is turbulence production occurring up to these frequencies. At depths of 15 mm and below, fluctuations on the order of 10^0–10^{-2} Hz (1 s–~15 min) have been reduced to zero. These spectra demonstrate that heat exchanged at the surface, as modulated by turbulent fluctuations, dynamically affects soil temperature in the uppermost mm of the soil even under a clear sky energy balance, i.e., without fluctuations in insolation caused by partly cloudy conditions. In addition to the rapid dampening of high-frequency fluctuations, the subsurface measurements also show an expected decrease of integral standard deviations with depth in the soil (Fig. 5b). The 0-mm thermocouple, placed directly at the uppermost grains of sand, shows good agreement with the remotely sensed surface temperature spectrum (Fig. 5a) and integral standard deviation (Fig. 5b). Figure 5b shows the integral standard deviation of air temperatures over the same period as vertical profiles, where acoustic temperature and DTS match well. Both the subsurface and atmospheric profiles show highest variability (diurnal amplitude) nearer the surface.
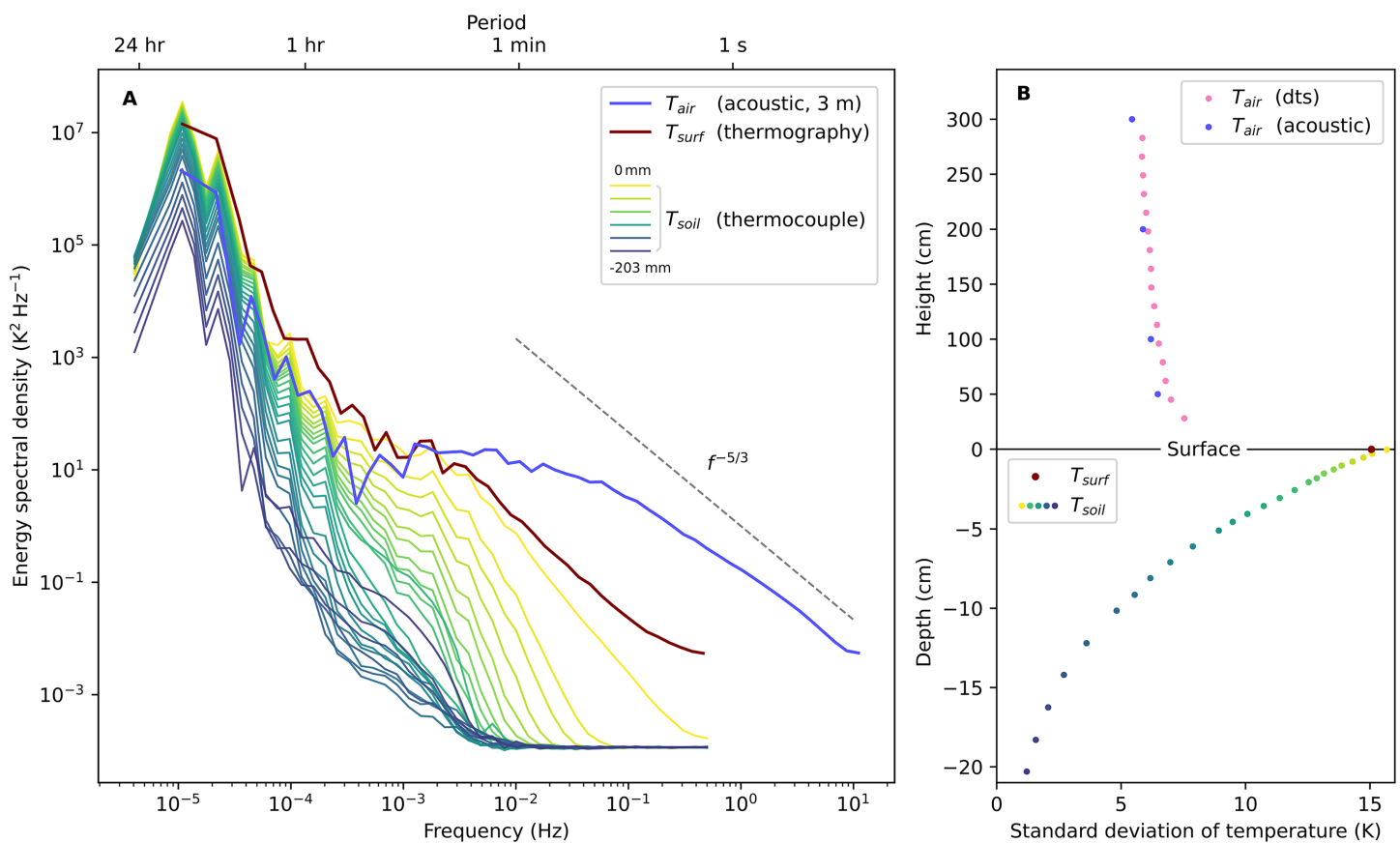

Fig. 5. (a) Temperature spectra from the 3-m sonic anemometer (T_{air}), an average spectrum calculated from 25 individual pixel spectra immediately adjacent to the soil site from the mast thermography (T_{surf}) and the soil thermocouples (T_{soil}). The sonic anemometer is used due to its faster frequency response and uninterrupted time series. Spectra are calculated from 14 Mar (T_{air}, T_{surf}) and 14–16 Mar (T_{soil}) to better illustrate the diurnal spectral peak. The line with slope −5/3 shows the inertial subrange of the turbulence cascade (Stull 1988). (b) Vertical profiles of the integral standard deviation over 24 h for the spectra presented in (a) as well as the DTS and additional sonic anemometers.

Space–time equivalence

Next, we move from one to three dimensions, using spatially distributed measurements to consider variance in the temperature field in both space and time (research goal 3). The DTS and surface thermography measurements allow us to explore the fundamental ergodic hypothesis applied to micrometeorological conditions: that under homogeneous and stationary situations, the space and time domains are interchangeable. This assumption is critical for eddy covariance theory because it allows a single point measurement integrated over time to be considered a valid representation of the average instantaneous spatial realization of the turbulent field (Kaimal and Finnigan 1994).
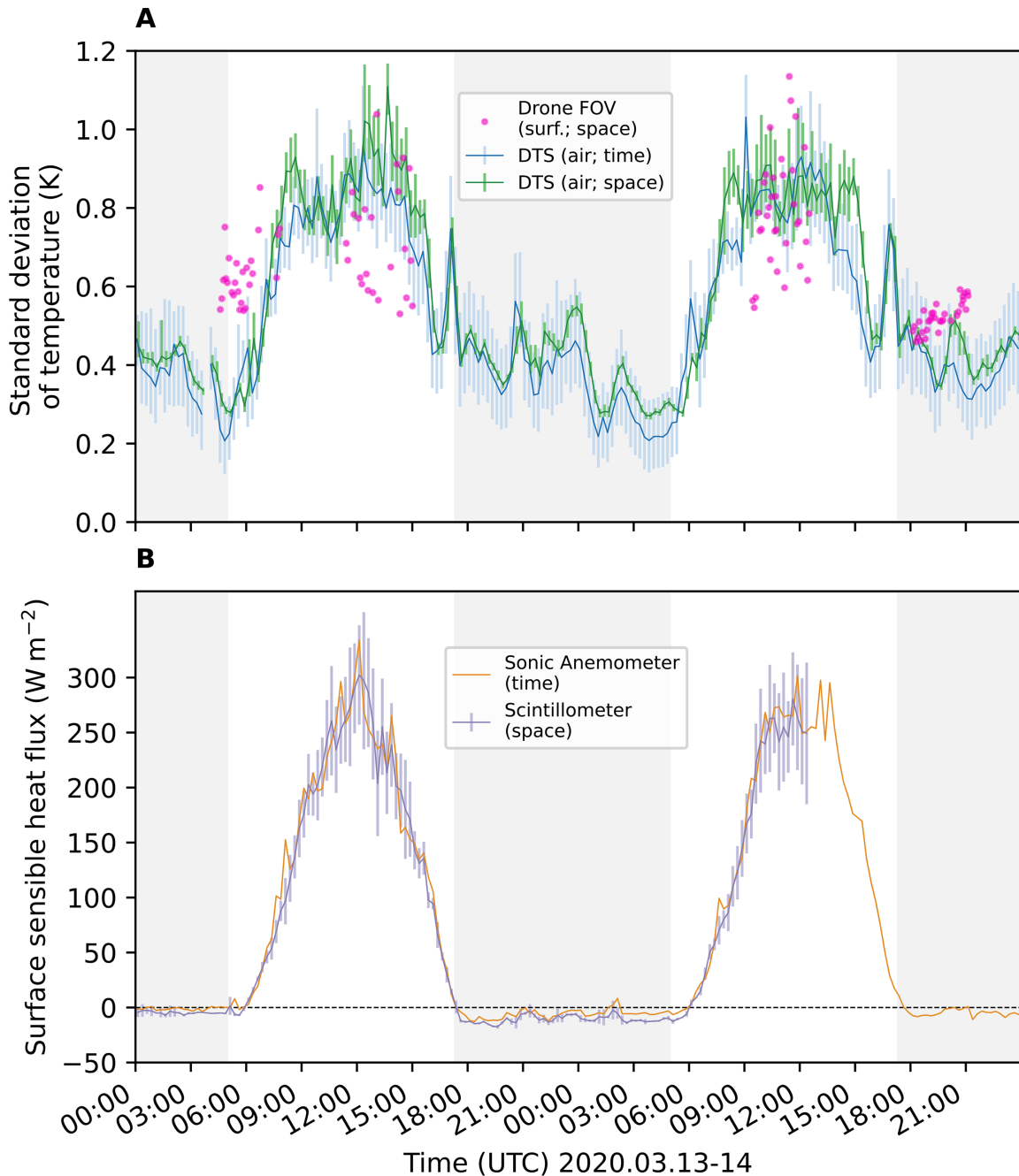

Fig. 6. (a) 15-min median σ_T in time (DTS, linearly detrended) and space (DTS, UAS FOV as shown in Fig. 2). Vertical bars are the 10th and 90th percentiles of each 15-min bin. (b) 15-min sensible heat fluxes measured from the 2.0-m sonic anemometer and the small-aperture scintillometer (mean 1-min flux ± 1 standard deviation for each 15-min period). Note that a power failure on 14 Mar limits the scintillometer time series to the first half of the day.

Using a single measurement height of the long DTS transects a standard deviation can be calculated in the space domain at each time step. Similarly, for each measurement point along the cable, and over some time interval, a standard deviation (σ_T) can be calculated in the time domain. A single height of the long transects contains 2,380 individual measurement points, and a 15-min period contains on average 690 sampling time steps. For each time step a spatial standard deviation was calculated and grouped into 15-min bins (average 690 spatial σ_T per period). Similarly, for each 15-min period and each measurement point, the time series was first linearly detrended and the standard deviation calculated (2,380 temporal σ_T per period). The diurnal course of the median standard deviation as well as the 10th and 90th percentiles are shown below in Fig. 6a for both space and time domains over two days. The variance due to instrument internal noise as measured in the calibration baths near the cable start has been subtracted. During the day, shadowing from the central mast will affect a small subset of DTS measurements, but given the extent of the array its influence is minor. If the time and space domains are interchangeable, we should expect 1:1 correspondence between the space and time σ_T measured by the DTS. An additional spatial σ_T is provided by the UAS-based thermal imager: for each flight conducted during 13 and 14 March, 10 frames (1.33 s, approximately equal to the DTS integration time) immediately following an internal shutter calibration were averaged, the thermal image clipped to the domain extent, and surface infrastructure (i.e., central mast, instrument platforms) were masked and a standard deviation calculated.

Generally, there is very good agreement between spatial and temporal σ_T from the DTS with regards to the diurnal course and through much of the period the measurements fall within each other's variability margins. Two distinct daytime periods of disagreement occur during 14 March, from 0730 to 0830 UTC and from 1400 to 1530 UTC, in which the spatial σ_T is significantly higher than the temporal σ_T. During 13 March the spatial σ_T is higher in both the morning period as well as from approximately 1200 to 1530 UTC. The source of this disagreement is not immediately clear, nor is the increase in both spatial and temporal σ_T just after 1600 UTC which appears to end with sunset on both days.

After midnight of 13 March and in the evening after 1930 UTC 14 March a consistently higher spatial σ_T is observed. These correspond broadly to periods of slower wind speeds (1–2 m s^{-1}) and suggest an increase in the spatial heterogeneity of temperatures. Even within the comparatively homogeneous NamTEX surface domain, variations in soil density or organic matter may affect local radiative cooling rates and create spatial distributions of warmer and cooler air that single point measurements are unable to quantify. Indeed, the instantaneous surface σ_T of the UAS-based thermography (pink dots) is often significantly greater (and increasing over time) during the period immediately after sunset on 14 March than either the spatial or temporal air temperature standard deviation. These results agree with previous research investigating spatial fluxes in suggesting that time averaging alone is not always able to capture the full spectrum of turbulent eddies (Mauder et al. 2008; Engelmann and Bernhofer 2016).

This interpretation is somewhat supported by Fig. 6b, which compares the surface sensible heat flux as measured at a point (sonic anemometer) and spatially averaged along a line (scintillometer). During the night, when the spatial σ_T of the DTS is higher, the small-aperture scintillometer consistently measures an absolute heat flux more than double that of the sonic anemometer: on average −9 W m^{-2} compared to −4 W m^{-2}. An interesting consequence relates to nocturnal energy balance closure: the sensible heat flux as measured by the scintillometer is able to account for a closure of 96% of the nocturnal surface energy balance, whereas the sonic anemometer heat flux provides 86% closure. While the absolute fluxes are small, this supports the hypothesis that in the stable nocturnal boundary layer spatial heterogeneities develop which are larger than the turbulent source area of eddy covariance measurements at a single point. This violates assumptions necessary for single-point measurement techniques to accurately capture the turbulent sensible heat flux. During the day, however, the fluxes
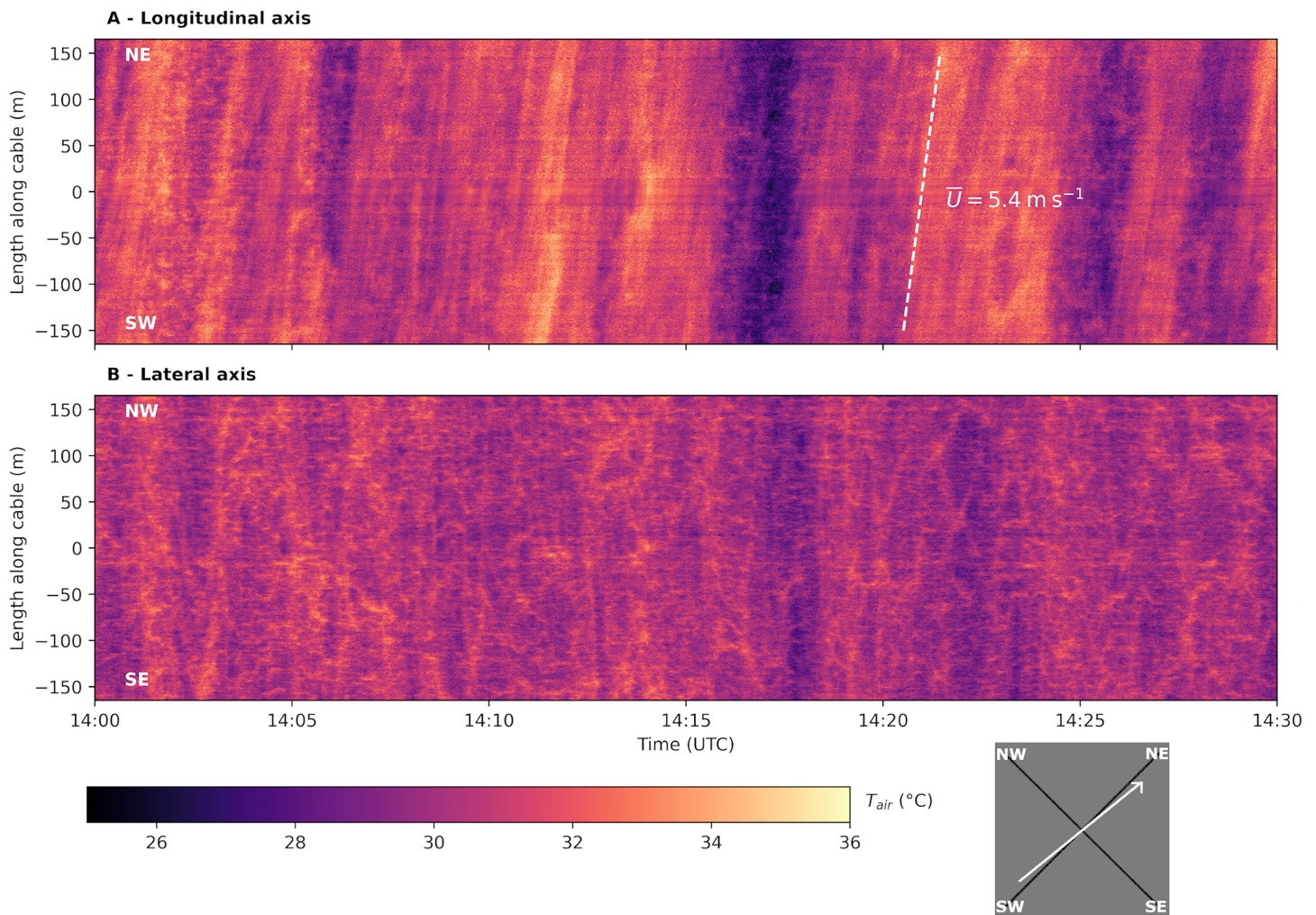
Fig. 7. DTS cable temperature at one measurement height (0.45 m) over a 30-min sampling period (1400–1430 UTC 14 Mar) for (a) the northeast–southwest axis and (b) the southeast–northwest axis. Each column represents one sample in time (*n* = 1395), each row a single measurement (0.254 m long) along the cable [*n* = 1299 (northeast–southwest), 1295 (northwest–southeast)]. At *y* = 0 the two transects intersect. Average Eulerian wind direction measured at the cable intersection by a sonic anemometer at 3.0 m AGL (white arrow, inset) over the period was 231° ± 10°. The corresponding average wind speed was 5.36 ± 1.1 m s^{-1} shown as the dashed white line [in (a); the *x*-axis location is arbitrary]. Persistent horizontal lines are where temperatures influenced by the fiber-optic support structure were removed and interpolated.

agree very well, with the scintillometer measuring 97% of the sonic anemometer fluxes. It must be noted, however, that the scaling relationships underpinning the scintillometer calculations were not developed in such extreme environments and different scaling functions can change the derived fluxes to a significant degree (Savage 2009). Additionally, due to the different measurement principles even the most carefully designed experiments will have differing source areas between collocated scintillometers and sonic anemometers.

Turbulence structure

The cross-shaped DTS array allows us to investigate the horizontal anisotropy of the spatial turbulent temperature field (research goal 4) directly. This provides an advantage over many tower-based studies in which the spatial and temporal domains are assumed to be interchangeable.

An example 30-min measurement period is shown in Fig. 7. Over this period the mean wind direction measured at the center of the domain was 231°; nearly parallel with the northeast–southwest DTS axis (Fig. 7a) and nearly orthogonal to the southeast–northwest axis (Fig. 7b). With moderate winds and unstable stratification this leads to a streaked pattern in the northeast–southwest axis as turbulent eddies travel along the length of the transect
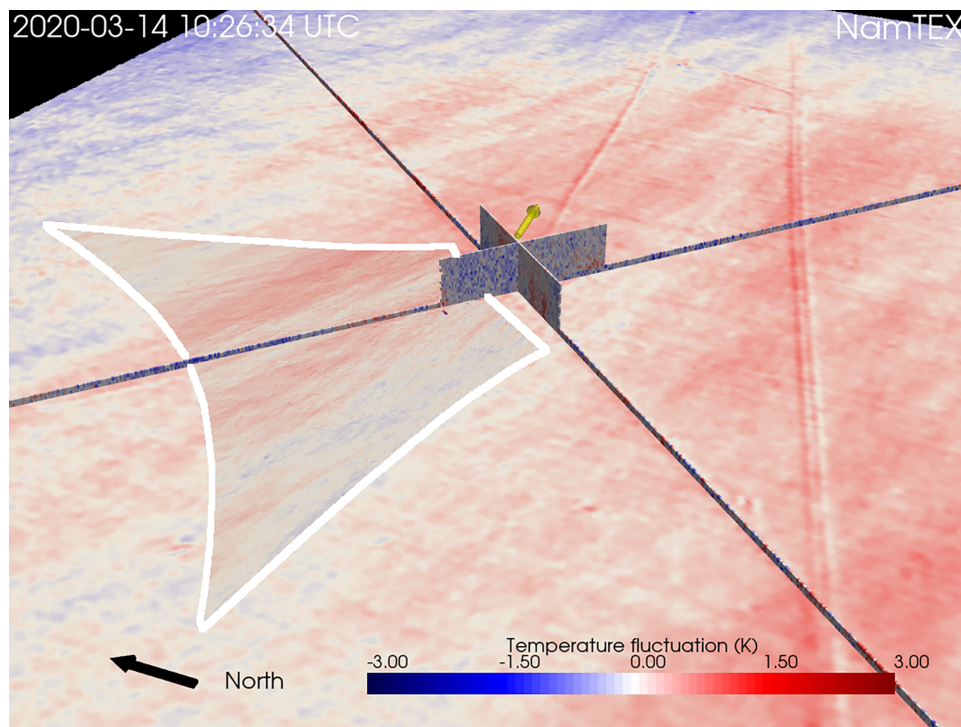
Fig. 8. Three-dimensional rendering of temperature fluctuations among nested measurement systems. The large surface is the FOV of the UAS thermography. The smaller inset surface (outlined in white) is the higher-resolution mast thermography. In vertical space the DTS measurements are shown with a 2× exaggerated vertical scale. The yellow arrow at the domain center shows the 1-s average wind direction measured by the 3-m sonic anemometer scaled to velocity. Full animation can be downloaded from the project Zenodo repository or streamed here: https://youtu.be/QLKU2-6oPJE.

(Fig. 7a). Such elongated structures are commonly observed in surface layer flows (Wilczak and Tillman 1980) as well as spatially resolved surface temperature perturbations (Garai and Kleissl 2013; Alekseychik et al. 2021). There is a noticeable angle to the structures, showing that they begin in the southwest and travel at some velocity in the direction of the cable. The mean wind velocity over the period of 5.4 m s^{-1} agrees well with the structure slope, and relative changes from this slope correlate with changes in wind velocity. Breaks in the streaks are related to changes in the wind velocity and direction within the domain: from Fig. 8 and the accompanying animation it is clear that wind direction is not always equal across the domain. The southeast–northwest axis (Fig. 7b) shows a lateral cross section and no preferential angle in its structures as the mean wind speed along this axis is approximately 0. The integral length scale suggests the structures are on average about 130 m long on the longitudinal axis and 35 m on the lateral axis. These two starkly different images are both samples of the same, simultaneously measured turbulent flow field, highlighting the structural horizontal anisotropy of the flow and importance of multidimensional observations.

Finally, we combine the surface and air temperature measurement systems in three-dimensional space. The decomposed surface thermography (see sidebar "Tracking turbulent motion with A-TIV") and DTS air temperature measurements display spatiotemporal fluctuations from the sample mean and thereby reveal the size, shape, and motion of turbulent structures passing through the domain as recorded by air temperature (DTS) and surface temperature (thermal imager) fluctuations.

The strong surface heating of the Namib results in turbulent temperature perturbations of ±3 K over this short (11 min) time series. The mean wind speed measured at the central mast was 3.7 ± 1.0 m s^{-1} and in these conditions the surface structures tended to elongate along the axis of travel.

Tracking turbulent motion with A-TIV

As individual turbulent structures in the ASL flow over the desert soil, they exchange heat at the surface and create rapid surface temperature fluctuations. To visualize and analyze these structures in the NamTEX thermography datasets, each pixel in a time series is converted from an instantaneous radiometric surface temperature T_{surf} (K) to a spatiotemporal temperature fluctuation T'_{surf} (K) by subtracting both the instantaneous spatial mean and the individual pixel time series mean from each measurement (Christen et al. 2012). The result of this process is shown in Fig. 8. To analyze the revealed flow, we employ the technique of thermal image velocimetry (TIV).

TIV is a computational image processing method that utilizes rapidly acquired (≥1 Hz) surface brightness temperature fluctuations from a thermal infrared camera to calculate thermal pattern velocity (Inagaki et al. 2013). TIV is analogous to particle image velocimetry in that the velocity and direction of thermal structures are determined from the correlation of a moving search window between consecutive frames. Adaptive thermal image velocimetry (A-TIV) is a new development that aims to automate the algorithm, eliminating user input and assimilating results across various averaging intervals that improves spatial velocity detection. This is done by applying a Hilbert–Huang transform (Huang et al. 1998), which is more suitable for nonstationary and nonlinear dynamics, on the raw brightness temperature field. The transform helps to identify the highest average instantaneous frequency in the dataset allowing the algorithm to adapt to high-frequency events found in different input thermal imagery. A-TIV also introduces the possibility to calculate a velocity field by means of multiple temporal running filter sizes to calculate the brightness temperature perturbation. On each precalculated brightness temperature perturbation dataset an entire TIV time series is calculated and subsequently merged using weighted averaging to create the final A-TIV product. This multiscale approach allows derivation of velocities over a wide range of surface types, from smooth surfaces to surfaces with individual roughness elements.

A strong temperature perturbation is necessary to extract high-frequency velocity vectors. Any individual A-TIV frame may contain many areas erroneously showing zero velocity if the underlying surface temperature fluctuations are below the detection limit of the algorithm. However, investigations of four UAS thermography flights have shown good agreement between the center 50 m × 50 m spatial average of the A-TIV velocities with the sonic anemometer tower measurement, providing cross-correlation values between 0.5 and 0.7 for each flight, with the highest correlation at the lowest (0.5 m) sonic anemometer and decreasing with height. A single frame of the A-TIV is shown in Fig. SB2 and an animation for the full flight is linked in the caption.

Further accuracy assessments are underway as well as a new approach to reconstruct vertical velocity from the A-TIV product using machine learning, which will further A-TIV's potential for spatial micrometeorological measurements.
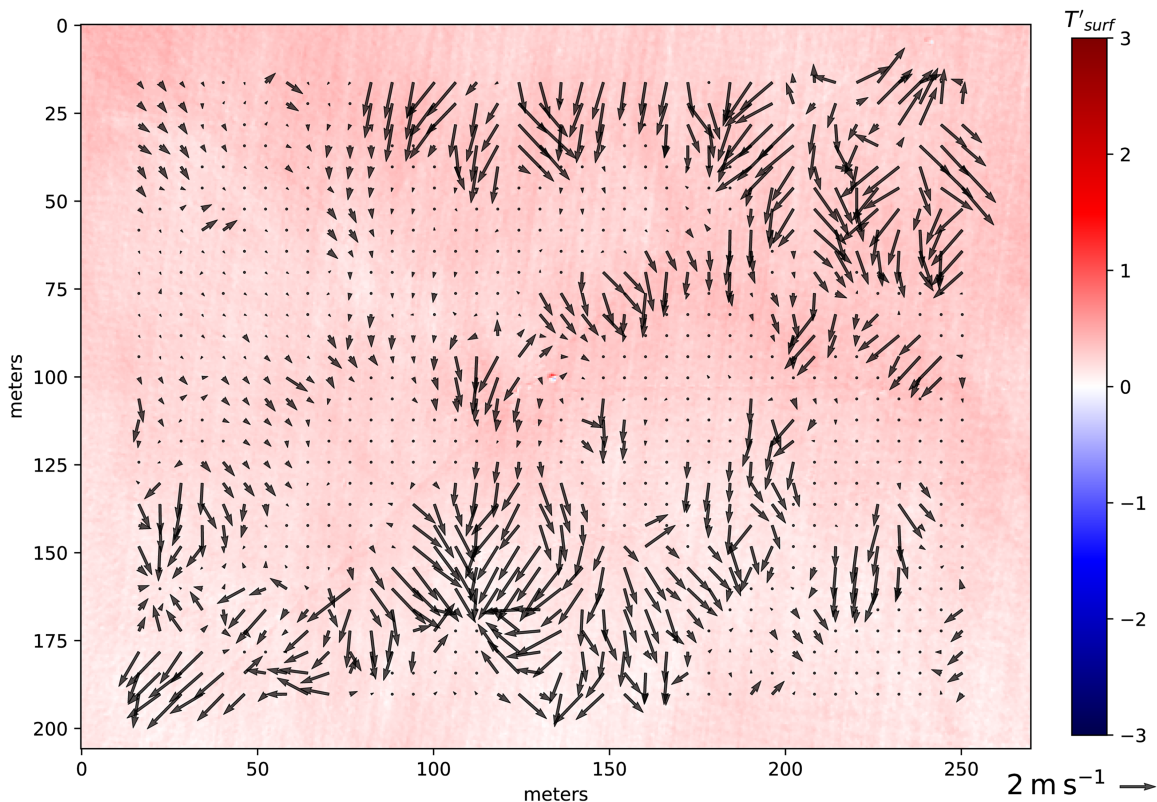

Fig. SB2. A-TIV product for one frame of the UAS-based thermography sampled at 0807:40 UTC 16 Mar. The background image shows the instantaneous temperature deviation from a spatiotemporal 60-s mean. Vectors display the movement of the respective pixel neighborhood for the iteration (384 s). The areas with no vectors shown are due to undetected movement between the calculation frames in this area. An animation of the full A-TIV product is available in the project Zenodo repository or to stream here: https://youtu.be/0JZpbQZKYXk.

The complex nature of the flow field is best exemplified in the accompanying animation. The mean flow toward the east-southeast is clear, and within this mean flow a rich spatiotemporal variation in turbulent direction and structure emerges, showing rapid changes in direction, patches of vorticity, and areas of apparent divergence and convergence at the surface. The cross arrangement of the DTS shows some of the vertical structure of the turbulence as it moves through the center of the domain. Combined with the soil temperatures from Figs. 4 and 5, these measurements also show that the traces of temperature fluctuations are found co-occurring in air, surface, and soil temperatures, and that these layers are coupled at the microscale. The increased detail provided by the mast-based thermography and ability to resolve finer-scale structures allows for a nested analysis of surface temperature fluctuations across a range between 300 m and ~0.5 cm. The complexity of the flow is apparent from a qualitative assessment. The sidebar "Tracking turbulent motion with A-TIV" explains one current approach to quantitatively assess the surface flow field. Of great interest is the possibility of extracting the convergence and divergence from the horizontal flow field to derive a vertical wind component due to mass balance that, if combined with temperature deviations, would allow an estimation of a spatially resolved sensible heat flux.

Summary and outlook

NamTEX combines a unique set of instrumentation and an ideal location for detailed investigation of heat transfer between the subsurface, surface, and atmosphere. The spatial distribution of measurements enables analysis from one to three dimensions and thereby investigation of several fundamental assumptions underlying many micrometeorology methods and the development of new approaches to quantify heat transfer.

In this preliminary analysis we showcased the potential of this dataset using a typical day during the campaign. In a 1D framework we considered air, surface, and subsurface temperatures, demonstrating that high-frequency temperature fluctuations are detectable in the subsurface (research goals 1 and 2). We then used the distributed temperature sensor as well as surface thermography to compare and contrast spatial and temporal temperature field standard deviations, demonstrating that there exist conditions under which the two disagree (research goals 1 and 3). Using spatially distributed temperature measurements we demonstrated that there exists significant horizontal anisotropy within instantaneous realizations and also the integral conditions of the horizontal flow field (research goal 4). Finally, the surface and atmospheric measurement systems were combined in three-dimensional space to visualize the scale, the dynamics, and the anisotropy of turbulent structures responsible for transporting heat between the surface and atmosphere. We demonstrated the co-occurrence of temperature fluctuations within the air, surface, and subsurface temperatures, showing the coupling of these three domains.

Ongoing and future work will focus on comprehensive investigations of the full observation period, and thorough investigation of questions raised by the four research goals. The morning and evening transition periods, the evolution of turbulent eddy structures through the day, and the relationship between the convective and Eulerian wind directions are especially interesting.

Data availability statement. The data used for the analysis presented in this article are available at the following Zenodo repository: https://doi.org/10.5281/zenodo.4729941. Further data will be released as the data processing of the campaign progresses. Updates can be followed by visiting the project homepage at https://www.meteo.uni-freiburg.de/en/research/namib-turbulence-experiment

References

Alekseychik, P., G. Katul, I. Korpela, and S. Launiainen, 2021: Eddies in motion: Visualizing boundary-layer turbulence above an open boreal peatland using UAS thermal videos. *Atmos. Meas. Tech.*, **14**, 3501–3521, https://doi.org/10.5194/amt-14-3501-2021.

Aubinet, M., T. Vesala, and D. Papale, 2012: *Eddy Covariance: A Practical Guide to Measurement and Data Analysis.* Springer, 365–376, https://doi.org/10.1007/978-94-007-2351-1.

Butterworth, B. J., and Coauthors, 2021: Connecting land–atmosphere interactions to surface heterogeneity in CHEESEHEAD19. *Bull. Amer. Meteor. Soc.*, **102**, E421–E445, https://doi.org/10.1175/BAMS-D-19-0346.1.

Cheng, Y., C. Sayde, Q. Li, J. Basara, J. Selker, E. Tanner, and P. Gentine, 2017: Failure of Taylor's hypothesis in the atmospheric surface layer and its correction for eddy-covariance measurements. *Geophys. Res. Lett.*, **44**, 4287–4295, https://doi.org/10.1002/2017GL073499.

Christen, A., F. Meier, and D. Scherer, 2012: High-frequency fluctuations of surface temperatures in an urban environment. *Theor. Appl. Climatol.*, **108**, 301–324, https://doi.org/10.1007/s00704-011-0521-x.

des Tombe, B., and B. Schilperoort, 2020: Dtscalibration Python package for calibrating distributed temperature sensing measurements (Version v1.0.2). Zenodo, https://doi.org/10.5281/zenodo.3876407.

——, ——, and M. Bakker, 2020: Estimation of temperature and associated uncertainty from fiber-optic Raman-spectrum distributed temperature sensing. *Sensors*, **20**, 2235, https://doi.org/10.3390/s20082235.

ECMWF, 1988: *Parameterization of Fluxes over Land Surface: Proceedings of a Workshop held at ECMWF, 24-26 October 1988.* ECMWF, 392 pp.

Engelmann, C., and C. Bernhofer, 2016: Exploring eddy-covariance measurements using a spatial approach: The eddy matrix. *Bound.-Layer Meteor.*, **161**, 1–17, https://doi.org/10.1007/s10546-016-0161-x.

Everard, K. A., H. J. Oldroyd, and A. Christen, 2020: Turbulent heat and momentum exchange in nocturnal drainage flow through a sloped vineyard. *Bound.-Layer Meteor.*, **175**, 1–23, https://doi.org/10.1007/s10546-019-00491-y.

Feigenwinter, C., J. Franceschi, J.A. Larsen, R. Spirig, and R. Vogt, 2020: On the performance of microlysimeters to measure non-rainfall water input in a hyper-arid environment with focus on fog contribution. *J. Arid Environ.*, **182**, 104260, https://doi.org/10.1016/j.jaridenv.2020.104260.

Garai, A., and J. Kleissl, 2011: Air and surface temperature coupling in the convective atmospheric boundary layer. *J. Atmos. Sci.*, **68**, 2945–2954, https://doi.org/10.1175/JAS-D-11-057.1.

——, and ——, 2013: Interaction between coherent structures and surface temperature and its effect on ground heat flux in an unstably stratified boundary layer. *J. Turbul.*, **14**, 1–23, https://doi.org/10.1080/14685248.2013.806812.

——, E. Pardyjak, G. J. Steeneveld, and J. Kleissl, 2013: Surface temperature and surface-layer turbulence in a convective boundary layer. *Bound.-Layer Meteor.*, **148**, 51–72, https://doi.org/10.1007/s10546-013-9803-4.

Garratt, J. R., and R. A. Pielke, 1989: On the sensitivity of mesoscale models to surface-layer parameterization constants. *Bound.-Layer Meteor.*, **48**, 377–387, https://doi.org/10.1007/BF00123060.

Göttsche, F.-M., and Coauthors, 2018: Fiducial Reference Measurements for validation of Surface Temperature from Satellites (FRM4STS): Report from the Field Inter-Comparison Experiment (FICE) for Land Surface Temperature. Rep. OFE-D130-LST-FICE-Report-V1-Iss-1-Ver-1, European Space Agency, 47 pp., www.frm4sts.org/wp-content/uploads/sites/3/2018/10/FRM4STS_LST-FICE_report_v2017-11-20_signed.pdf.

Higgins, C. W., M. Froidevaux, V. Simeonov, N. Vercauteren, C. Barry, and M. Parlange, 2012: The effect of scale on the applicability of Taylor's frozen turbulence hypothesis in the atmospheric boundary layer. *Bound.-Layer Meteor.*, **143**, 379–391, https://doi.org/10.1007/s10546-012-9701-1.

——, M. G. Wing, J. Kelley, C. Sayde, J. Burnett, and H. A. Holmes, 2018: A high resolution measurement of the morning ABL transition using distributed temperature sensing and an unmanned aircraft system. *Environ. Fluid Mech.*, **18**, 683–693, https://doi.org/10.1007/s10652-017-9569-1.

Horst, T. W., J. Kleissl, D. H. Lenschow, C. Meneveau, C.-H. Moeng, M. B. Parlange, P. P. Sullivan, and J. C. Weil, 2004: HATS: Field observations to obtain spatially filtered turbulence fields from crosswind arrays of sonic anemometers in the atmospheric surface layer. *J. Atmos. Sci.*, **61**, 1566–1581, https://doi.org/10.1175/1520-0469(2004)061<1566:HFOTOS>2.0.CO;2.

Huang, N. E., and Coauthors, 1998: The empirical mode decomposition and the Hilbert spectrum for nonlinear and non-stationary time series analysis. *Proc. Roy. Soc. London*, **A454**, 903–995, https://doi.org/10.1098/rspa.1998.0193.

Inagaki, A., M. Kanda, S. Onomura, and H. Kumemura, 2013: Thermal image velocimetry. *Bound.-Layer Meteor.*, **149**, 1–18, https://doi.org/10.1007/s10546-013-9832-z.

Kaimal, J. C., and J. J. Finnigan, 1994: *Atmospheric Boundary Layer Flows – Their Structure and Measurement.* Oxford University Press, 289 pp., https://doi.org/10.1002/qj.49712152512.

Keller, C. A., H. Huwald, M. K. Vollmer, A. Wenger, M. Hill, M. B. Parlange, and S. Reimann, 2011: Fiber optic distributed temperature sensing for the determination of the nocturnal atmospheric boundary layer height. *Atmos. Meas. Tech.*, **4**, 143–149, https://doi.org/10.5194/amt-4-143-2011.

Lothon, M., and Coauthors, 2014: The BLLAST field experiment: Boundary-Layer Late Afternoon and Sunset Turbulence. *Atmos. Chem. Phys.*, **14**, 10931–10960, https://doi.org/10.5194/acp-14-10931-2014.

Mauder, M., and T. Foken, 2004: Documentation and Instruction Manual of the Eddy Covariance Software Package TK2. Arbeitsergebnisse 26, Universität Bayreuth, Abt. Mikrometeorolofgie, 45 pp., https://epub.uni-bayreuth.de/884/1/ARBERG026.pdf.

——, R. L. Desjardins, E. Pattey, Z. Gao, and R. van Haarlem, 2008: Measurement of the sensible eddy heat flux based on spatial averaging of continuous ground-based observations. *Bound.-Layer Meteor.*, **128**, 151–172, https://doi.org/10.1007/s10546-008-9279-9.

——, T. Foken, and J. Cuxart, 2020: Surface-energy-balance closure over land: A review. *Bound.-Layer Meteor.*, **177**, 395–426, https://doi.org/10.1007/s10546-020-00529-6.

Mendelsohn, J., A. Jarvis, C. Roberts, and T. Robertson, 2002: *Atlas of Namibia: A Portrait of the Land and its People.* Sunbird Publishers, 200 pp.

Morrison, T. J., M. Calaf, H. J. S. Fernando, T. A. Price, and E. R. Pardyjak, 2017: A methodology for computing spatially and temporally varying surface sensible heat flux from thermal imagery. *Quart. J. Roy. Meteor. Soc.*, **143**, 2616–2624, https://doi.org/10.1002/qj.3112.

——, ——, C. W. Higgins, S. A. Drake, A. Perelet, and E. Pardyjak, 2021: The impact of surface temperature heterogeneity on near-surface heat transport. *Bound.-Layer Meteor.*, **180**, 247–272, https://doi.org/10.1007/s10546-021-00624-2.

Peltola, O., K. Lapo, I. Martinkauppi, E. O'Connor, C. K. Thomas, and T. Vesala, 2021: Suitability of fibre-optic distributed temperature sensing for revealing mixing processes and higher-order moments at the forest-air interface. *Atmos. Meas. Tech.*, **14**, 2409–2427, https://doi.org/10.5194/amt-14-2409-2021.

Savage, M. J., 2009: Estimation of evaporation using a dual-beam surface layer scintillometer and component energy balance measurements. *Agric. For. Meteor.*, **149**, 501–517, https://doi.org/10.1016/j.agrformet.2008.09.012.

Sayde, C., C. K. Thomas, J. Wagner, and J. Selker, 2015: High-resolution wind speed measurements using actively heated fiber optics. *Geophys. Res. Lett.*, **42**, 10064–10073, https://doi.org/10.1002/2015GL066729.

Schilperoort, B., M. Coenders-Gerrits, W. Luxemburg, C. J. Rodríguez, C. C. Vaca, and H. Savenije, 2018: Technical note: Using distributed temperature sensing for Bowen ratio evaporation measurements. *Hydrol. Earth Syst. Sci.*, **22**, 819–830, https://doi.org/10.5194/hess-22-819-2018.

Schols, J. L., 1984: The detection and measurement of turbulent structures in the atmospheric surface layer. *Bound.-Layer Meteor.*, **29**, 39–58, https://doi.org/10.1007/BF00119118.

Schumacher, B., M. Katurji, J. Zhang, I. Stiperski, and C. Dunker, 2019: Evolution of micrometeorological observations: Instantaneous spatial and temporal surface wind velocity from thermal image processing. *Geocomputation Conf. 2019*,

Queenstown, New Zealand, University of Auckland, 23 pp., https://doi.org/10.17608/k6.auckland.9869942.v1.

Selker, J. S., and Coauthors, 2006: Distributed fiber-optic temperature sensing for hydrologic systems. *Water Resour. Res.*, **42**, W12202, https://doi.org/10.1029/2006WR005326.

Sigmund, A., L. Pfister, C. Sayde, and C. K. Thomas, 2017: Quantitative analysis of the radiation error for aerial coiled-fiber-optic distributed temperature sensing deployments using reinforcing fabric as support structure. *Atmos. Meas. Tech.*, **10**, 2149–2162, https://doi.org/10.5194/amt-10-2149-2017.

Spirig, R., and Coauthors, 2019: Probing the fog life cycles in the Namib desert. *Bull. Amer. Meteor. Soc.*, **100**, 2491–2507, https://doi.org/10.1175/BAMS-D-18-0142.1.

Stull, R., 1988: *An Introduction to Boundary Layer Meteorology.* Springer, 670 pp., https://doi.org/10.1007/978-94-009-3027-8.

Thiermann, V., and H. Grassl, 1992: The measurement of turbulent surface-layer fluxes by use of bichromatic scintillation. *Bound.-Layer Meteor.*, **58**, 367–389, https://doi.org/10.1007/BF00120238.

Thomas, C. K., and J. Selker, 2021: Optical-fibre-based distributed sensing methods. *Handbook of Atmospheric Measurements*, T. Foken, Ed., Springer, 609–631, https://doi.org/10.1007/978-3-030-52171-4_20.

——, A. M. Kennedy, J. S. Selker, A. Moretti, M. H. Schroth, A. R. Smoot, N. B. Tufillaro, and M. J. Zeeman, 2012: High-resolution fibre-optic temperature sensing: A new tool to study the two-dimensional structure of atmospheric surface-layer flow. *Bound.-Layer Meteor.*, **142**, 177–192, https://doi.org/10.1007/s10546-011-9672-7.

Tong, C., 1996: Taylor's hypothesis and two-point coherence measurements. *Bound.-Layer Meteor.*, **81**, 399–410, https://doi.org/10.1007/BF02430337.

Tyson, P. D., and M. K. Seely, 1980: Local winds over the central Namib. *S. Afr. Geogr. J.*, **62**, 135–150, https://doi.org/10.1080/03736245.1980.10559630.

Ward, H. C., 2017: Scintillometry in urban and complex environments: A review. *Meas. Sci. Technol.*, **28**, 064005, https://doi.org/10.1088/1361-6501/aa5e85.

Wilczak, J. M., and J. E. Tillman, 1980: The three-dimensional structure of convection in the atmospheric surface layer. *J. Atmos. Sci.*, **37**, 2424–2443, https://doi.org/10.1175/1520-0469(1980)037<2424:TTDSOC>2.0.CO;2.

Wilson, J. D., 2013: Statistics of the wind-speed difference between points with cross-wind separation. *Bound.-Layer Meteor.*, **146**, 149–160, https://doi.org/10.1007/s10546-012-9763-0.

Xian, X., W. Tao, S. Qingwei, and Z. Weimin, 2002: Field and wind-tunnel studies of aerodynamic roughness length. *Bound.-Layer Meteor.*, **104**, 151–163, https://doi.org/10.1023/A:1015527725443.

Zeeman, M. J., J. S. Selker, and C. K. Thomas, 2015: Near-surface motion in the nocturnal, stable boundary layer observed with fibre-optic distributed temperature sensing. *Bound.-Layer Meteor.*, **154**, 189–205, https://doi.org/10.1007/s10546-014-9972-9.

Zeller, M.-L., J.-M. Huss, L. Pfister, K. E. Lapo, D. Littmann, J. Schneider, A. Schulz, and C. K. Thomas, 2021: The NY-Ålesund TurbulencE Fiber Optic eXperiment (NYTEFOX): investigating the Arctic boundary layer, Svalbard. *Earth Syst. Sci. Data*, **13**, 3439–3452, https://doi.org/10.5194/essd-13-3439-2021.